



## Microstructure and load sensitive fatigue crack nucleation in Ti-6242 using accelerated crystal plasticity FEM simulations

Somnath Ghosh<sup>a,\*</sup>, Pritam Chakraborty<sup>b</sup>

<sup>a</sup> Department of Civil Engineering, Johns Hopkins University, United States

<sup>b</sup> Department of Mechanical Engineering, The Ohio State University, United States

### ARTICLE INFO

#### Article history:

Received 31 July 2012

Received in revised form 19 October 2012

Accepted 23 October 2012

Available online 16 November 2012

#### Keywords:

Fatigue crack nucleation

Wavelets

Multi-time scaling

Crystal plasticity FEM

### ABSTRACT

This paper investigates microstructure and load sensitive fatigue behavior of Ti-6242 using cyclic crystal plasticity finite element (CPFE) simulations of statistically equivalent image-based microstructures. A wavelet transformation induced multi-time scaling (WATMUS) method [1,2] is used to perform accelerated cyclic CPFE simulations till crack nucleation, otherwise infeasible using conventional time integration schemes. A physically motivated crack nucleation model in terms of crystal plasticity variables [3] is extended in this work to predict nucleation. The crack nucleation model is based on dislocation pile-up and stress concentration at grain boundaries, caused by inhomogeneous plastic deformation in the polycrystalline microstructure. The model is calibrated and validated with experiments. The dependence of yield strength on the underlying grain orientations and sizes is developed through the introduction of an effective microstructural parameter *Plastic Flow Index* or *PFI*. To determine the effects of the microstructure on crack nucleation, a local microstructural variable is defined in terms of the surface area fraction of soft grains surrounding each hard grain or *SAFSSG*. Simulations with different cyclic load patterns suggest that fatigue crack nucleation in Ti-6242 strongly depends on the dwell cycle hold time at maximum stress.

© 2012 Elsevier Ltd. All rights reserved.

### 1. Introduction

The fatigue life and number of cycles to crack nucleation in commercially used titanium alloys, such as Ti-6242, exhibit considerable variation at room temperature [4]. This is due to the influence of heterogeneities in the underlying microstructure on deformation and fatigue characteristics [5–7]. Mechanistic approaches, implementing crystal plasticity-based finite element (CPFE) simulations of polycrystalline microstructures, have been pursued in the literature [4,8–12] to develop fatigue life models. These mechanistic approaches are more accurate than conventional lifing methods, where the microstructural influence on fatigue life is accommodated through phenomenological models obtained from extensive testing of specimens [13–18].

At room temperature, inelastic deformation in Ti-6242 commences predominantly by slip on different slip systems in individual grains of the microstructure [5–7]. The number of slip systems and their resistance to slip depends on the morphological and crystallographic characteristics. For instance in the *hcp* phase of Ti-6242, the three basal and prismatic (*a*) slip systems have much lower slip resistances in comparison with the six *a* pyramidal, 12 *c + a* first order pyramidal and six *c + a* second order pyramidal

slip systems [19–21]. Consequently, grains with orientations that induce higher resolved shear stresses on the basal or prismatic systems have more plastic deformation than those activating the pyramidal systems. This material anisotropy due to the large difference in critical resolved shear stress in different slip systems results in large heterogeneity in the plastic deformation in polycrystalline aggregates. It leads to significant load-shedding induced stress concentration at grain boundaries. This is perceived to be the primary driver of microstructure-dependent crack nucleation [5,22].

The present work uses a size and rate-dependent CPFE model of Ti-6242 developed in [19,20,23] to capture this load-shedding induced stress rise in the microstructure leading to crack nucleation. Particularly vulnerable are boundaries between grains having large time-dependent plastic deformation (soft grain) and those with little or no plasticity (hard grain) owing to their orientation with respect to the loading direction. Morphological and crystallographic features of the polycrystalline alloy are statistically represented in the CPFE models using methods developed in [24,25]. The use of such a statistical description not only reduces the number of grains in the FE simulations but also captures the key features of the microstructure that affect its macroscopic and microscopic response. A non-local crack nucleation model has been developed in [3] to study early crack nucleation in polycrystalline Ti-alloys under dwell fatigue cyclic loading. The crack nucleation criterion is functionally dependent on stress concentration and dislocation pile-up at grain boundaries. These variables are obtained

\* Corresponding author. Address: 3400 N, Charles Street, Baltimore, MD 21218, United States. Tel.: +1 410 516 7833; fax: +1 410 516 7473.

E-mail address: [sghosh20@jhu.edu](mailto:sghosh20@jhu.edu) (S. Ghosh).

from CPFEM simulations. A combination of CPFE simulations and ultrasonic testing of dwell fatigue Ti-6242 samples has been used in [3] for calibrating and validating the nucleation model. This model is adopted and slightly extended in the present work to study microstructure and load dependent crack nucleation in Ti-6242. While the overall framework is applicable to different crack nucleation criteria, the present results are valid for the criteria adopted.

Although CPFE simulations accurately capture the deformation behavior of polycrystalline alloys, they require very small time steps when conventional time integration schemes are used to march forward in time. In cyclic loading and deformation, small time steps in every cycle of the loading process leads to prohibitively large computations, when analysis is performed for a large number of cycles to fatigue failure. To overcome this limitation, fatigue life predictions have been performed in [26,4,27] by extrapolating the results based on CPFE simulations performed for few cycles. However extrapolation can lead to considerable error in the evolution of *local* microstructural variables and cause inaccurate fatigue life prediction. Accurate life prediction requires cycle-by-cycle evolution of all microstructural variables in cyclic CPFEM simulations till the failure event.

Evolution of CPFE variables under cyclic loading has two distinct time scales, viz. (i) fine time scale corresponding to the high frequency oscillations of the applied loading and (ii) coarse time scale corresponding to the low frequency evolution of material relaxation. Multi-time scaling methods may be devised to decouple this dual-time behavior and perform time integration only for the coarse time-scale problem with the lower frequency response. The *wavelet transformation induced multi-time scaling* or WATMUS method, developed in [1,2], has shown significant computational benefits in rapidly traversing a high number of cycles. The WATMUS method is distinctly advantageous over other multi-time scale schemes such as the method of separation of motions [28,29], asymptotic expansion based methods [30,31] or almost periodic temporal homogenization operator based method [32,33], where inherent scale separation and local periodicity or almost periodicity in temporal evolution are assumed. Such assumptions are invalid for crystal plasticity variables, which show strong non-periodic evolution and spatio-temporal localization. The WATMUS method does not make these assumptions and is used in the present work to perform accelerated cyclic CPFEM simulations.

This paper is intended to understand the effects of microstructure and cyclic loading conditions on grain-level crack nucleation. The WATMUS method based cyclic CPFE simulations of polycrystalline Ti-6242 microstructures are used to accomplish this mechanistic approach. An overview of the CPFE model is presented in Section 2. The crack nucleation model developed in [3] is discussed in Section 3. The WATMUS method is described in Section 4 along with some examples to demonstrate its efficiency and accuracy. Calibration and validation of the crack nucleation model parameters for dwell fatigue using CPFE simulations and experiments are conducted in Section 5. A detailed numerical study of the different factors affecting fatigue crack nucleation in Ti-6242 is executed in Section 6. In Section 6.2, relations between crystallographic features and cycles to crack nucleation are developed. The dependence on the number of cycles to crack nucleation on characteristics of the applied load is studied in Section 6.3.

## 2. Size and rate dependent crystal plasticity FE model for Ti-6242

The rate and size dependent crystal plasticity constitutive laws governing deformation in polycrystalline, bi-phasic Ti-6242 alloys have been developed in detail in [19,20,23,34]. The total deforma-

tion gradient is assumed to be multiplicatively split into an elastic and plastic part [35,36] as:

$$\mathbf{F} = \mathbf{F}^e \mathbf{F}^p \quad (1)$$

The elastic part of the deformation gradient  $\mathbf{F}^e$  captures the stretching and rotation of the lattice, whereas the plastic deformation is due to crystallographic slip on different slip systems. It is expressed from the relation

$$\dot{\mathbf{F}}^p \mathbf{F}^{p-1} = \sum_{\alpha} \dot{\gamma}^{\alpha} \mathbf{S}_0^{\alpha} \quad (2)$$

where  $\dot{\gamma}^{\alpha}$  is the slip rate on different slip systems and  $\mathbf{S}_0^{\alpha}$  is the Schmid tensor expressed in terms of the slip direction  $\mathbf{m}_0^{\alpha}$  and slip plane normal  $\mathbf{n}_0^{\alpha}$  in an intermediate configuration. A power law model described in [36,37] is used to determine the slip-rate on different slip systems as:

$$\dot{\gamma}^{\alpha} = \dot{a} \left| \frac{\tau^{\alpha} - \chi^{\alpha}}{g^{\alpha}} \right|^{\frac{1}{m}} \text{sign}(\tau^{\alpha} - \chi^{\alpha}) \quad (3)$$

where  $\dot{a}$  is a reference slip rate,  $\tau^{\alpha}$  is the resolved shear stress on the slip system,  $\chi^{\alpha}$  is a back stress,  $g^{\alpha}$  is the slip system resistance and  $m$  is the power law exponent. The resolved shear stress on a slip system is obtained from

$$\tau^{\alpha} = \mathbf{F}^{eT} \mathbf{F}^e \mathbf{T}^* : \mathbf{S}_0^{\alpha} \quad (4)$$

where  $\mathbf{T}^*$  is the 2nd Piola–Kirchhoff (PK2) stress. A hyper-elastic law is used to obtain the PK2 stress from the work conjugate Lagrange–Green strain tensor  $\mathbf{E}^e (= \frac{1}{2}(\mathbf{F}^{eT} \mathbf{F}^e - \mathbf{I}))$  as:

$$\mathbf{T}^* = \mathbf{C} : \mathbf{E}^e \quad (5)$$

where  $\mathbf{C}$  is the elastic stiffness tensor. The back stress evolution on a slip system follows the law:

$$\dot{\chi}^{\alpha} = c \dot{\gamma}^{\alpha} - d \chi^{\alpha} |\dot{\gamma}^{\alpha}| \quad (6)$$

where  $c$  and  $d$  are the direct hardening and dynamic recovery coefficients respectively [38].

The evolution of slip system deformation resistance is controlled by two types of dislocations, viz. statistically stored dislocations (SSDs) and geometrically necessary dislocations (GNDs) (see [3]). SSD's correspond to homogeneous plastic deformation, while GND's accommodate incompatibility of the plastic strain field due to lattice curvature, especially near grain boundaries. The corresponding deformation resistance rate is expressed as:

$$\dot{g}^{\alpha} = \sum_{\beta} h^{\alpha\beta} |\dot{\gamma}^{\beta}| + \frac{k_0 \hat{\alpha}^2 G^2 b}{2(g^{\alpha} - g_0^{\alpha})} \sum_{\beta} \lambda^{\beta} |\dot{\gamma}^{\beta}| \quad (7)$$

The first term in Eq. (7) corresponds to SSDs. The modulus  $h^{\alpha\beta} = q^{\alpha\beta} h^{\beta}$  (no sum on  $\beta$ ) is the strain hardening rate due to self and latent hardening on the  $\alpha$ -th slip system by slip on the  $\beta$ -th slip system respectively. Here,  $h^{\beta}$  is the self hardening self hardening coefficient and  $q^{\alpha\beta}$  is a matrix describing latent hardening. The microstructure of Ti-6242 consists of primary  $\alpha$  grains and transformed  $\beta$  colonies. The primary  $\alpha$  grains have a *hcp* crystal lattice structure, while the transformed  $\beta$  colonies consist of alternate laths of *hcp* lattice and symmetric *bcc* lattice. Different self hardening relationships are used for modeling the  $\alpha$  and  $\beta$  phases [20]. The evolution of self hardening for the  $\alpha$  phase is modeled as:

$$h^{\alpha} = h_0^{\alpha} \left| 1 - \frac{g^{\alpha}}{g_s^{\alpha}} \right|^r \text{sign} \left( 1 - \frac{g^{\alpha}}{g_s^{\alpha}} \right) \quad (8)$$

$$g_s^{\alpha} = \hat{g} \left| \frac{\dot{\gamma}^{\alpha}}{\dot{a}} \right|^c$$

where  $h_0^{\alpha}$  is a reference self hardening parameter and  $g_s^{\alpha}$  is the saturation value of slip system resistance. Self hardening rate of the  $\beta$  phase is given as:

$$h^z = h_s^z + \operatorname{sech}^2 \left[ \frac{h_0^z - h_s^z}{\tau_s^z - \tau_0^z} \gamma^{acc} \right] (h_0^z - h_s^z) \quad (9)$$

$$\gamma^{acc} = \int_0^t \sum_{\alpha} |\dot{\gamma}^{\alpha}| dt$$

$h_0^z$  and  $h_s^z$  are the initial and asymptotic hardening rates,  $\tau_s^z$  represents the saturation value of shear stress when  $h_s^z = 0$ , and  $\gamma^{acc}$  is the accumulated plastic slip on the slip system.

The second term in Eq. (7) accounts for the effect of GNDs on work hardening developed in [39]. Here,  $k_0$  is a dimensionless material constant,  $G$  is the elastic shear modulus,  $b$  is the Burgers vector,  $g_0^z$  is the initial deformation resistance and  $\hat{\alpha}$  is a non-dimensional constant.  $\hat{\alpha}$  is taken to be  $\frac{1}{3}$  in [3].  $\lambda^{\beta}$  is a measure of slip plane lattice incompatibility, which can be expressed for each slip system slip system as a function of slip plane normal  $\mathbf{n}^{\beta}$  and an incompatibility tensor  $\mathcal{A}$  as:

$$\lambda^{\beta} = (\mathbf{A}\mathbf{n}^{\beta} : \mathbf{A}\mathbf{n}^{\beta})^{\frac{1}{2}} \quad (10)$$

The dislocation density tensor  $\mathcal{A}$  can be expressed using the curl of plastic deformation gradient tensor  $\mathbf{F}^p$ .

To avoid explicit modeling of the alternating lath structure of transformed  $\beta$  colonies in the CPFEM simulations of polycrystalline Ti-6242, an equivalent homogenized model has been proposed in [20]. The primary reason for homogenization of the colony response was to make simulation of polycrystalline microstructures tractable with computationally reasonable degrees of freedom. The equivalent model has a total of 78 slip systems corresponding to the *hcp* and *bcc* slip systems of the  $\alpha$  and  $\beta$  phases respectively. It is based on a mixture rule, where the individual phases at a material point are subject to a homogeneous deformation gradient  $\mathbf{F}$ , giving rise to different stresses and plastic variables in each of the phases. The homogenized stress is obtained from the weighted sum of the stresses based on volume fractions of individual phases in the colony as:

$$\boldsymbol{\sigma} = w_{\alpha}\boldsymbol{\sigma}_{\alpha} + w_{\beta}\boldsymbol{\sigma}_{\beta} \quad (11)$$

The weights  $w_{\alpha}$  and  $w_{\beta}$  correspond to the volume fractions of individual phases of these alloys. The approach provides a good approximation of the local deformation state at grain/colony boundaries, but not at higher resolutions of the intra-colony  $\alpha/\beta$  interfaces. While this homogenization has some limitations with respect to local response prediction of fatigue crack nucleation, it is expected to provide a reasonably good estimation of the location of the crack nucleation site at a lower resolution of grains.

The effect of grain size and lath thickness on the slip system resistance is also considered in the crystal plasticity model in [23]. A Hall Petch type relation is used to modify the initial slip system resistances  $g^{\alpha}(t=0)$  to capture size effect according to the relation:

$$g^{\alpha}(t=0) = g_0^{\alpha} + \frac{K^{\alpha}}{\sqrt{D^{\alpha}}} \quad (12)$$

where  $g_0^{\alpha}$  is the homogeneous slip system resistance,  $D^{\alpha}$  is a characteristic length parameter that corresponds to the mean-free path of the dislocations in a grain. For globular  $\alpha$  grains, the transmission of dislocations to adjacent grains is resisted by grain boundaries and hence grain diameter is considered as characteristic length in Eq. (12). For transformed  $\beta$  colonies, dislocation motions can be impeded either by the colony boundary or lath boundary depending on the Burger's orientation relation between  $\alpha$  and  $\beta$  laths [19,20]. Hence either colony size or lath thickness is used for  $D^{\alpha}$  in Eq. (12) for slip system resistances of the transformed  $\beta$  colonies.  $K^{\alpha}$  is a constant that depends on the Poisson's ratio, shear modulus, Burgers vector and barrier strength. The different parameters in the model have been calibrated from experiments on single crystal

Ti-6Al and Ti-6242 in [19,20,23]. Similar values of critical resolved shear stresses have been obtained from micro-cantilever bending experiments performed on single crystal  $\alpha$ -Titanium alloys in [21].

Analysis of the microstructural influence on deformation and creep behavior requires statistically equivalent polycrystalline microstructures in CPFEM simulations. Statistically equivalent microstructures of polycrystalline alloys have been constructed from distributions of grain size, shape, orientation, misorientation, and microtexture in [24,25]. Simulations in [3,23] have demonstrated that hard grains surrounded by soft regions develop large stresses near their boundaries, which keep increasing with time due to rate effects.

### 3. Non-local crack nucleation model for near $\alpha$ Ti-alloys

A crack nucleation model, developed in [3], is used in this work to model grain-level nucleation in a polycrystalline ensemble. The model has been motivated from experimental observations of failed Ti-6242 samples under room temperature dwell-fatigue loading with a maximum stress of 90–95% of yield strength, and stress ratio  $\sigma_{min}/\sigma_{max} = 0$  [40,41]. Experimentally extracted crystallographical features of grains at failure sites suggest that regions of hard grains surrounded by soft grains are susceptible to initiate a crack [41,3]. During the hold period of the loading, soft grains with favorably oriented  $\langle a \rangle$ -type slip systems for dislocation glide undergo significant plastic straining. Contiguous hard grains with less-favorably oriented for  $\langle a \rangle$ -type slip ( $c$ -axis parallel to the deformation direction), experience large local stress concentrations, especially near the shared grain boundary. This is a consequence of compatible, large elastic strains in the hard grains near the shared boundary. The phenomenon of rising stress-concentration with evolving creep strains in dwell cycles has been called load shedding [19,3]. The hard grain crack nucleation criterion, ahead of dislocation pile-ups in adjacent soft grain has been derived to be [3]:

$$T_{eff} = \sqrt{\langle T_n \rangle^2 + \beta T_t^2} \geq \frac{K_c}{\sqrt{\pi c}} \quad (13)$$

or equivalently

$$R = T_{eff} \cdot \sqrt{c} \geq R_c, \quad \text{where } R_c = \frac{K_c}{\sqrt{\pi}} \quad (14)$$

In Eqs. (13) and (14),  $T_{eff}$  is an effective traction on the hard grain basal plane for mixed mode crack nucleation. It is expressed in terms of the stress component normal to the crack surface  $T_n = \boldsymbol{\sigma}_{ij} n_j^b$  and the tangential stress component  $T_t = \|\mathbf{T} - T_n \mathbf{n}^b\|$ . Here  $\mathbf{T}$  is the stress vector on the crack surface,  $\boldsymbol{\sigma}_{ij}$  is the Cauchy stress tensor and  $n_j^b$  are the components of unit outward normal to the crack surface. Only the tensile normal stress  $\langle T_n \rangle$ , represented by the McCauley bracket  $\langle \cdot \rangle$ , contributes to the effective stress responsible for crack opening.  $K_c$  is the critical mixed-mode stress intensity factor and  $\beta \approx K_{nc}/K_{tc}$  is a shear stress factor used to assign different weights to the normal and shear traction components for mixed-mode. A value of  $\beta = 0.7071$  is used for Ti-64 alloys in this study.  $c$  is the length of a wedge micro-defect or crack on the basal plane of the hard grain caused by dislocation pile-up in the adjacent soft grain. A schematic of a micro-crack of length  $c$  on the basal plane of a hard grain, the corresponding dislocation pile-up  $\mathbf{B}$  in the adjacent soft grain and the local effective traction  $T_n$ ,  $T_t$  at the crack nucleation site is shown in Fig. 1. The critical crack nucleation parameter  $R_c$  in Eq. (14) is a material property, which is calibrated from experiments.

The micro-crack length  $c$  in Eq. (14) is obtained from the relation proposed in [42] as:

$$c = \frac{G}{8\pi(1-\nu)\gamma_s} B^2 \tag{15}$$

where  $B$  is the crack opening displacement,  $G$  is the shear modulus,  $\nu$  is the Poisson's ratio and  $\gamma_s$  is the surface energy. The crack opening displacement  $B = \|\mathbf{B}\|$  is a non-local variable that is evaluated from the equation:

$$\mathbf{B} = \int_{\Omega} \mathbf{\Lambda} \cdot \mathbf{n} d\Omega = \int_{\Omega} (\nabla^T \times \mathbf{F}^p) \cdot \mathbf{n} d\Omega \tag{16}$$

Here  $\mathbf{n}$  is normal to surface  $\Omega$  in which the Burgers circuit is considered,  $\mathbf{\Lambda}$  is Nye's dislocation tensor and  $\nabla$  is the curl operator. The numerical procedure to evaluate the evolving crack nucleation parameter ( $R_\alpha$ ) at a node  $\alpha$  on the grain boundary is described in [3].

**4. Wavelet transformation based multi-time scale (WATMUS) method for accelerated cyclic CPFEM simulations**

Fatigue life predictions in polycrystalline metallic microstructures involve cyclic crystal plasticity FEM simulations till crack nucleation. Depending on the microstructure and load profile, this may involve simulations for large number of cycles. Such simulations may become computationally prohibitive using conventional time integration schemes in FEM codes. In [1,2], a wavelet transformation based multi-time scale or WATMUS method has been developed to reduce the problem to a set of low frequency, coarse time-scale governing equations. In the WATMUS scheme, any time dependent variable  $v^\zeta(t)$  is expressed as:

$$v^\zeta(t) = v(N, \tau) = \sum_{k=1}^n v_k(N) \psi_k(\tau) \quad \forall \tau \in [0, T] \tag{17}$$

The superscript  $\zeta$  corresponds to the dependence of the variable on the two time-scales, which for this problem correspond to a cycle scale  $N$  and an intra-cycle fine time-scale  $\tau$ .  $\psi_k(\tau)$  are wavelet basis functions that capture the high frequency response within each cycle,  $n$  is the number of basis functions required for accurate representation of the waveform. Compact support, multi-resolution and orthogonality properties of the wavelet basis functions [43,44] allow significant reduction in the number of basis functions required for accurate representation of arbitrary waveforms in different evolving variables. The compact or finite support of the wavelet basis functions also eliminates spurious oscillations that may arise with truncation of terms in infinitely supported basis functions such as the spectral basis functions.  $v_k(N)$  are the associated coefficients that evolve monotonically in the cycle ( $N$ )-scale. Using orthogonality property, they may be expressed as:

$$v_k(N) = \frac{1}{T} \int_0^T v(N, \tau) \psi_k(\tau) d\tau \tag{18}$$

where  $T$  is time period of the applied load. Wavelet transformation facilitates numerical integration of the CPFEM equations in the cy-

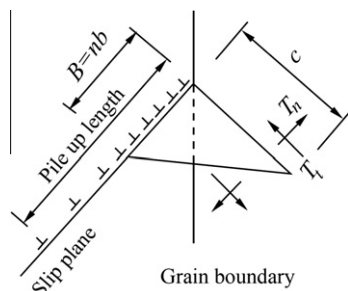


**Fig. 1.** Schematic of a wedge micro crack formation resulting from dislocation pile-up in the soft grain near a hard soft grain boundary, where  $c$  is the micro crack length and  $B = \|\mathbf{B}\|$  is the crack opening displacement due to dislocation pile-up.

cle-scale traversing several cycles in each step. This leads to significant efficiency gain.

The cycle-scale weak form for the FEM micromechanics problem of the polycrystalline microstructure, in the absence of inertia terms, is obtained by substituting Eq. (17) in the semi-discrete system of equations. The resulting transformed system of equations to be solved for the wavelet coefficients at each node  $\alpha$  is given as:

$$\begin{aligned} R_{i,k}^\alpha(N) &= \frac{1}{T} \int_0^T R_i^\alpha(N, \tau) \psi_k d\tau \\ &= \sum_e \int_{V_{0,e}} \frac{1}{T} \int_0^T \frac{\partial P^\alpha}{\partial X_j} \sigma_{ji} \psi_k d\tau dV_{0,e} \\ &\quad - \sum_{S_T} \int_{S_0} \frac{1}{T} \int_0^T P^\alpha t_{jA} \psi_k d\tau dS_0 = 0 \end{aligned} \tag{19}$$

where  $P^\alpha$  are the FE shape functions in every element  $e$ ,  $S_T$  are the surfaces on which tractions are applied,  $\alpha$  are the nodes of the discretized domain,  $V_{0,e}$  and  $S_0$  are the element volumes and surfaces in the reference configuration respectively and  $\sigma_{ji}$  are the stresses at integration points in the spatially discretized domain. The transformed weak form (19) is solved at discrete cyclic increments using a Quasi-Newton iterative scheme for the wavelet coefficients of nodal displacements  $C_{i,k}^\alpha$ :

$$C_{i,k}^\alpha(N) = \frac{1}{T} \int_0^T u_i^\alpha(N, \tau) \psi_k(\tau) d\tau \tag{20}$$

$u_i^\alpha$  are the nodal displacement degrees of freedom in the finite element model. The oscillatory stress response  $\sigma_{ji}(N, \tau)$  in Eq. (19) depends on the oscillatory deformation gradient  $F_{ij}(N, \tau)$  and internal variables  $y_m(N, \tau)$ .  $F_{ij}(N, \tau)$  at each integration point in any cycle is obtained from the coefficients of nodal displacements  $C_{i,k}^\alpha(N)$  using the relation:

$$F_{ij}(N, \tau) = \delta_{ij} + \frac{\partial P^\alpha}{\partial X_j} \sum_{k=1}^n C_{i,k}^\alpha(N) \psi_k(\tau) \tag{21}$$

In crystal plasticity, the evolution of internal variables is governed by first order rate equations of the type

$$\dot{y}_m^\zeta(t) = f_m(y_m^\zeta, F_{ij}^\zeta, t) \tag{22}$$

Here  $y_m^\zeta$  are internal variables represented in a single time-scale  $t$  and  $f_m$  are non-linear functions. The oscillatory evolution of the dual-scale variable  $y_m(N, \tau)$  in any cycle may be obtained from the fine-scale time integration as:

$$y_m(N, \tau) = y_{m0}(N) + \int_0^\tau f_m(y_m, F_{ij}, N, \tau) d\tau \tag{23}$$

where  $y_{m0}(N) = y_m(N, \tau = 0)$  are values of internal variables at the beginning of a cycle. This forms a new cycle-scale variable, corresponding to the initial values of internal variables  $y_{m0}$ , which have a monotonic evolution in the cycle-scale. Cycle-scale rate equations are numerically defined for  $y_{m0}$  as [1]:

$$\frac{\partial y_{m0}}{\partial N} = y_{m0}(N + 1) - y_{m0}(N) = y_m(N, T) - y_{m0}(N) \tag{24}$$

where

$$y_m(N, T) = y_{m0}(N) + \int_0^T f_m(y_m, F_{ij}, N, \tau) d\tau \tag{25}$$

Since  $f_m$  are non-linear functions, numerical time-integration using the backward Euler scheme is performed on Eq. (25). The cycle-scale internal variables are integrated using a 2nd order backward difference formula, expressed as:

$$y_{m0}(N) = \beta_1 y_{m0}(N - \Delta N) - \beta_2 y_{m0}(N - \Delta N - \Delta N_p) + \beta_3 \left. \frac{\partial y_{m0}}{\partial N} \right|_N \Delta N$$

where  $\beta_1 = \frac{(r+1)^2}{(r+1)^2 - 1}$   $\beta_2 = \frac{1}{(r+1)^2 - 1}$

$$\beta_3 = \frac{(r+1)^2 - (r+1)}{(r+1)^2 - 1} \text{ and } r = \frac{\Delta N_p}{\Delta N} \quad (26)$$

The Newton–Raphson iterative scheme is used to solve Eq. (26).

Adaptive methodologies have been developed in [1] to improve the efficiency and reduce the number of degrees of freedom in the WATMUS method. Only those wavelet coefficients of nodal displacements that evolve, are selected and retained in the function representations. Subsequently, the optimal set of equations are solved in a cyclic increment using the cycle-scale weak form of Eq. (19). Additionally an optimal cycle-stepping condition is derived for improving computational efficiency. Optimal cycle-steps are predicted from an upper bound of the truncation error in the 2nd order backward difference formula used to integrate the cycle scale internal variables. The use of these adaptive criteria significantly enhances the performance of WATMUS method for cyclic CPFEM simulations.

#### 4.1. A slightly modified WATMUS scheme to accommodate larger time periods

The WATMUS algorithm proposed in [1] is suitable for problems where the time period of applied load is relatively small. This is due to the fact that the entire oscillatory response over a cycle is represented by a single set of multi-resolution wavelet basis functions. This deteriorates the resolution when large time periods are involved, often encountered in dwell fatigue simulations. To alleviate this shortcoming, the total time period is divided into smaller segments with different maximum resolutions. The maximum resolution in every segment is determined from the first few cycles of a single time-scale simulation. This structure is not altered in the cycle-scale simulation. The use of different maximum resolutions drastically reduces the total number of wavelet coefficients that needs to be stored and also expedites the fine time-scale integration to obtain the cycle-scale rate equations of internal variables  $y_{m0}$ .

#### 4.2. Evaluation of accuracy and efficiency of WATMUS method by normal cyclic fatigue simulation of Ti-6242 microstructure

The accuracy of the WATMUS method is demonstrated by comparing the evolution of crystal plasticity variables obtained from (i) single time-scale, and (ii) WATMUS method-enhanced dual time-scale simulations of a statistically equivalent virtual polycrystalline Ti-6242 microstructure [24,25]. In Fig. 2, the microstructure is subjected to a triangular cyclic load on the  $y$ -face with a maximum and minimum normal traction of 869 MPa and 0 MPa respectively, and a time period of 2 s.

The WATMUS method-enhanced CPFEM simulation is performed for 300,000 cycles and the evolutionary variables, e.g. set of wavelet coefficients of nodal displacements  $C_{i,k}^x$  and the history of coarse scale internal variables  $\mathbf{y}_0^{z/\beta} = \{F_{ij,0}^p, g_0^z, \chi_0^z\}$  are compared with a single time-scale simulation. The single time-scale simulation suffers from a large computational overhead, and the simulation is performed for 215 cycles only. A comparison of the evolution of coarse internal variables at an integration point in the microstructure is shown in Fig. 3. The relative error  $e_0(N) = \frac{|\tilde{y}_0(N) - y_0(N)|}{|y_0(N)|}$  in the evolution of the coarse internal variables ( $\tilde{y}_0$ -WATMUS and  $y_0$ -single time scale) at an integration point in

the microstructure is shown in Fig. 4. The figures show rapid convergence with increasing cycles.

Highly resolved fine time-scale response within any cycle can be reconstructed from the cycle-scale variables in the WATMUS-based CPFEM simulations using the wavelet basis functions in Eq. (17). The relative error in the WATMUS-reconstructed fine time-scale evolution of internal variables, with respect to pure single time scale results is defined as:

$$e(N, \tau) = \frac{|\tilde{y}(N, \tau) - y(N, \tau)|}{\|y(N, \tau)\|} \quad (27)$$

where  $\tilde{y}(N, \tau)$  is reconstructed from the cycle-scale variables using the wavelet basis functions and  $y(N, \tau)$  is the single time-scale solution. The relative error for different variables at an element integration point in the microstructure at the 211th cycle is depicted in Fig. 5.

The distribution of the loading direction stress  $\sigma_{22}$  along a specified material line in the microstructure, as obtained by the WATMUS and single time scale simulations is compared in the Fig. 6.

These comparisons conclusively show that the WATMUS method is able to capture the evolution of the local microstructural variables very accurately. Finally to demonstrate the power of the WATMUS method in traversing a large number of cycles, the evolution of plastic deformation gradient  $F_{0,22}^p$  with advancing cycles are shown in Fig. 7 for up to 300,000 cycles.

The corresponding evolution of stress  $\sigma_{22}$  in the 300,000th cycle at the fine time-scale  $\tau = 0$  and  $\tau = 1$  s are shown in Fig. 8.

To evaluate the computational efficiency, the CPU time to perform 215 cycles for the single time-scale CPFEM simulation is extrapolated to 300,000 cycles and compared with the CPU time taken to perform 300,000 cycles of WATMUS simulation. A computational speedup of  $\sim 100$  times is obtained for this problem.

#### 4.3. WATMUS method based dwell fatigue simulation of Ti-6242 microstructure

The ability of the WATMUS method in handling large time periods is demonstrated through a dwell fatigue simulation for the polycrystalline microstructure shown in Fig. 2. A schematic of the dwell load with 2 min hold and the corresponding segments are shown in Fig. 9a and b respectively.

The cycle-scale evolution of  $F_{0,22}^p$  and  $g_0^z$  for a slip system at an integration point in the microstructure by the WATMUS method-enhanced CPFEM simulation is shown in Fig. 10.

The monotonic evolution of  $F_{0,22}^p$  and contour plots of its distribution are shown in Fig. 11.

The evolution of  $\sigma_{22}$  along a material line in the microstructure is evaluated for the cycles 21 and 500, at  $\tau = 121$  s, and is depicted in Fig. 12. Large stresses develop in the hard grains adjacent to soft grains due to anisotropy, leading to orientation dependent rate of plastic deformation and load-shedding. The stress peak rises with advancing cycles of the load, thus enhancing the probability of crack nucleation in these hard grains.

The WATMUS method-enhanced CPFE simulations is used in conjunction with the crack nucleation model in Section 3 to study the fatigue nucleation behavior of Ti-alloys.

### 5. Calibration and validation of critical crack nucleation parameter $R_c$

The critical crack nucleation parameter  $R_c$  should be calibrated prior to conducting crack nucleation sensitivity analyses using CPFE simulations. Subsequent validation studies are performed using 2 different specimens of the Ti-6242 alloy, subject to dwell fatigue load with a hold time of 2 min, and loading and unloading

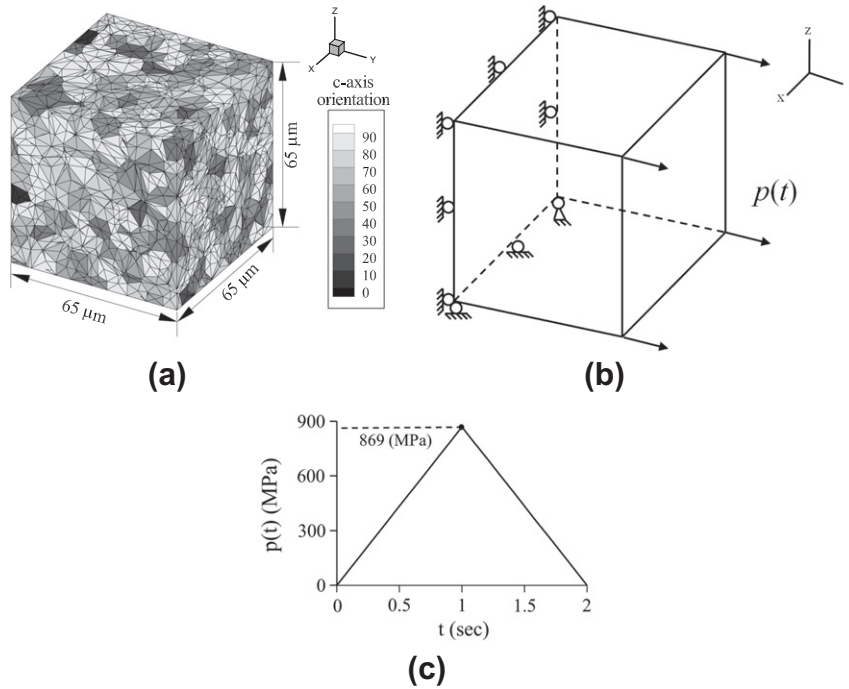


Fig. 2. FE model of a polycrystalline microstructure and loading conditions to demonstrate the accuracy and efficiency of the WATMUS method: (a) microstructure with (c)-axis orientation and mesh, (b) boundary conditions, and (c) cyclic loading profile.

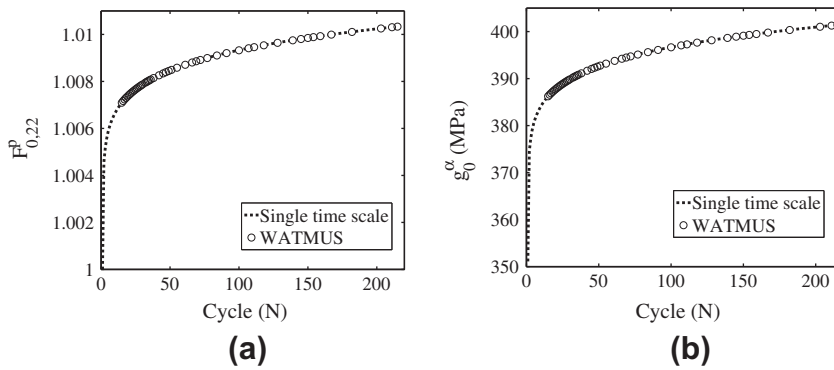


Fig. 3. Comparison of the evolution of the cycle-scale with averaged single time-scale internal variables at an integration point in the FE model of the polycrystalline microstructure for: (a)  $F_{0.22}^p$ , (b)  $g_0^\alpha$ .

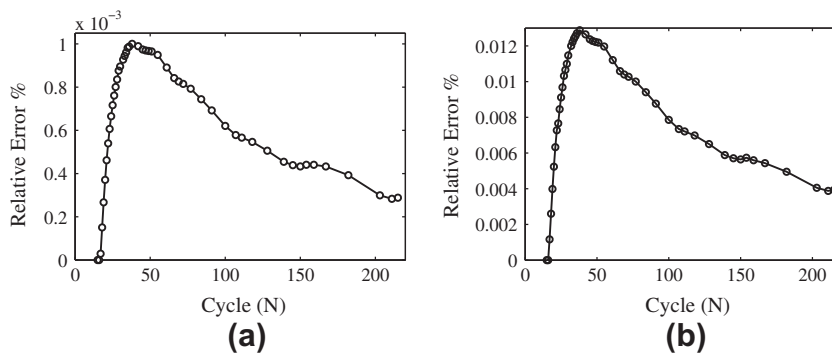
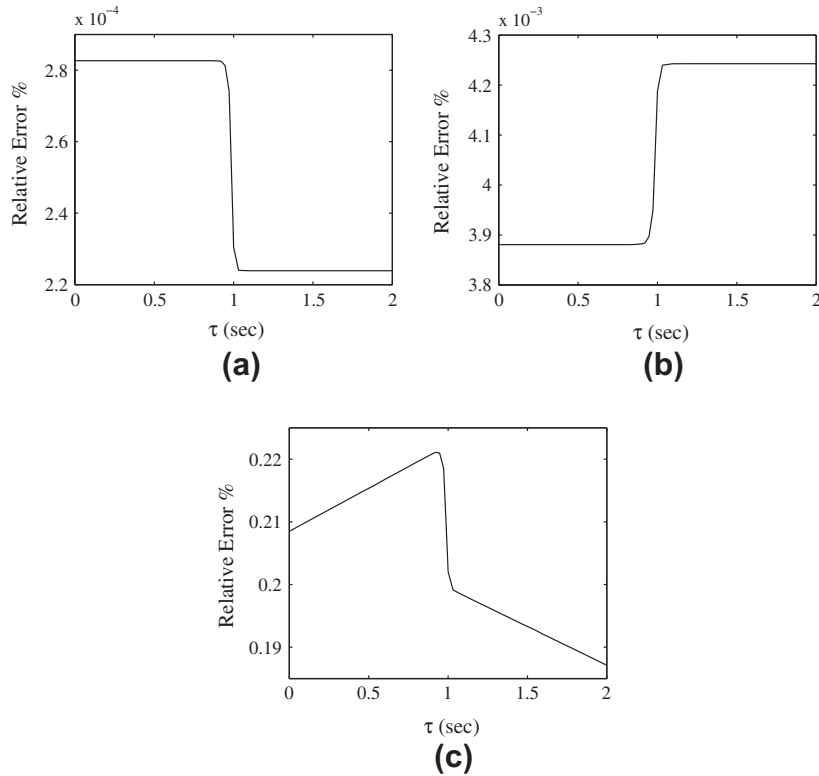


Fig. 4. Relative error  $e_0(N) = \frac{|\bar{y}_0(N) - y_0(N)|}{|y_0(N)|}$  between the cycle-scale and average of single time-scale internal variables: (a)  $F_{0.22}^p$  and (b)  $g_0^\alpha$ , at an integration point in the polycrystalline FE model.

time of 1 s each. The maximum stress in a loading cycle is 869 MPa, which is 95% of the yield strength, while the minimum stress is

0 MPa. Subsurface crack propagation has been monitored by using micro-radiographic images from interrupted experiments in [45].



**Fig. 5.** Relative error  $e(N, \tau) = \frac{|y(N, \tau) - y(N, \tau)|}{\|y(N, \tau)\|}$  of fine scale evolution of variables at 211th cycle at an integration point in the FE model of the polycrystalline microstructure for: (a)  $F_{22}^p$ , (b)  $g^z$ , (c)  $\sigma_{22}$ .

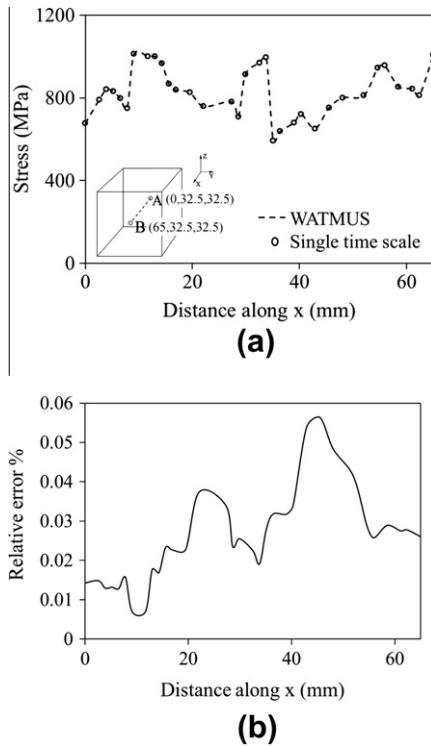


**Fig. 6.** Comparison of distribution of stress  $\sigma_{22}$  along a material line in the microstructure at  $N = 211$  and  $\tau = 1$  s, by the WATMUS and single time-scale CPFEM simulations for: (a)  $\sigma_{22}$  (b) relative error in  $\sigma_{22}$ .

The lengths of the dominant cracks are progressively recorded and plotted as shown in Fig. 13. The number of cycles to initiate a crack is estimated by extrapolating the curve to zero crack length.

From dwell fatigue experiments on Ti-6242 specimens, it has been observed in [45] that crack nucleation occurs at 80–85% of the total number of cycles to failure  $N_f$ . The evolution of a crack with cycles for the specimen 2, along with the extrapolated functional fit, are shown in Fig. 13.

5.1. Statistically equivalent microstructures

CPFEM simulation specimens of statistically equivalent polycrystalline microstructures are generated from orientation imaging microscopy (OIM) scans of the Ti-6242 microstructure. Following developments in [24,25,46], distribution and correlation functions of various crystallographic and morphological parameters, e.g. orientation, misorientation, microtexture, grain size, etc. from OIM scans of material specimens are used to generate statistically equivalent image based microstructures. The resulting microstructures for specimens 1 and 2 are shown in Fig. 14. Their  $\langle c \rangle$ -axis orientation distribution and microtexture are shown in Fig. 15.

5.2. Evaluating yield strengths and dwell fatigue simulations

The overall yield strengths of the specimens 1 and 2 in the loading direction are evaluated from constant strain rate simulations prior to dwell fatigue simulations. These values are required for applied load control at 95% of the yield strength in dwell-fatigue tests. The evolution of volume averaged stress-true strain in the loading direction  $\sigma_{22}-\epsilon_{22}$  are shown in Fig. 16. Corresponding to 0.2% elastic strain, an yield strength value of  $\sim 915$  MPa is assessed for these specimens.

The WATMUS method-enhanced CPFEM simulations are performed under dwell loading for validating the crack nucleation model. Consistent with experimental procedures, a maximum applied stress of 869 MPa, which corresponds to 95% of the yield

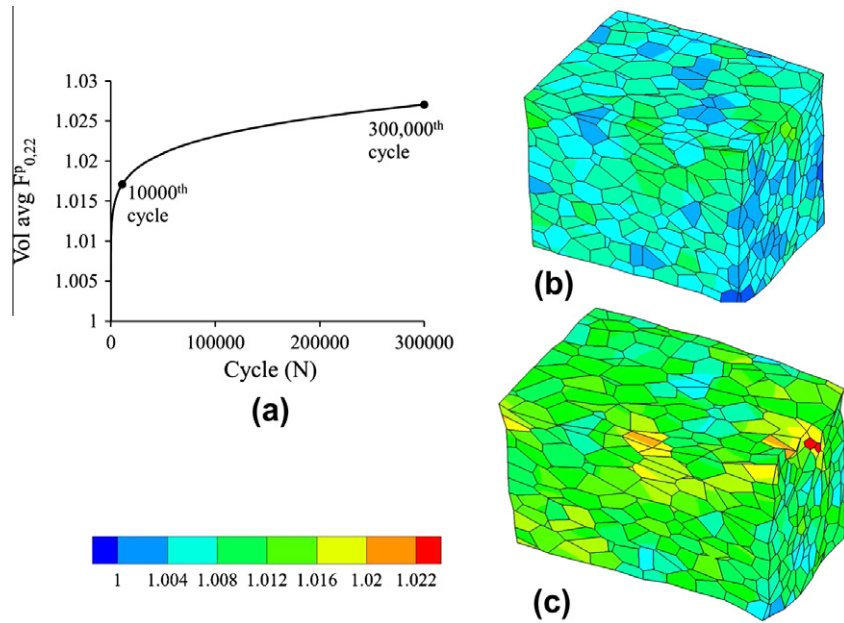


Fig. 7. Evolution of  $F_{0,22}^p$  with cycles by WATMUS-based CPFEM simulation: (a) volume averaged  $F_{0,22}^p$ , (b) distribution of  $F_{0,22}^p$  at the 10,000th cycle, and (c) distribution of  $F_{0,22}^p$  at the 300,000th cycle.

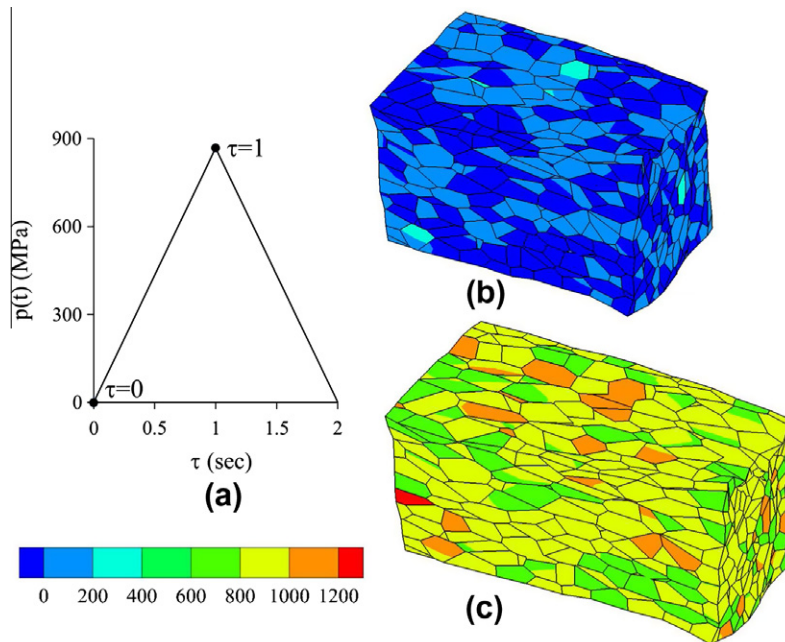


Fig. 8. Evolution of fine time-scale  $\sigma_{22}$  at the 300,000th cycle by WATMUS-based CPFEM simulation: (a) applied load profile on the  $y$ -face of the microstructure, (b) distribution of  $\sigma_{22}$  at  $\tau = 0$  s, (c) distribution of  $\sigma_{22}$  at  $\tau = 1$  s.

stress, and a stress ratio  $\sigma_R = \sigma_{min}/\sigma_{max} = 0$  is applied. Following the procedure described in [3], the crack nucleation parameter  $R_x$  at every node on grain interfaces is evaluated at  $\tau = 121$  s in each cycle for the 2-min dwell.

Experimental results of specimen 1, which fails after 352 cycles, are used to calibrate  $R_c$ . From the conclusions of experimental studies in [45], the minimum and maximum number of cycles to crack nucleation for the specimen 1 is estimated as  $N_{c(80\%)} = 282$  (80% of  $N_f$ ) and  $N_{c(85\%)} = 300$  (85% of  $N_f$ ). The evolution of the nodal  $R_x$  at the grain boundaries is obtained from CPFEM simulations of specimen 1. The maximum  $R_x$  values at  $N_{c(80\%)} = 282$  and

$N_{c(80\%)} = 300$  are considered as the lower and upper limits of  $R_c$  respectively.

$$R_{c(80\%)} = \max_x R_x(N = 282, \tau = 121 \text{ s}) = 6.54 \text{ MPa } \sqrt{\mu\text{m}}$$

$$R_{c(85\%)} = \max_x R_x(N = 300, \tau = 121 \text{ s}) = 6.80 \text{ MPa } \sqrt{\mu\text{m}} \quad (28)$$

The evolution of  $R_x(N, \tau = 121 \text{ s})$  with cycles at the predicted crack nucleation site is shown in Fig. 17.

Experimental results of specimen 2 are used to validate the crack nucleation model for the calibrated  $R_c$  value. The number

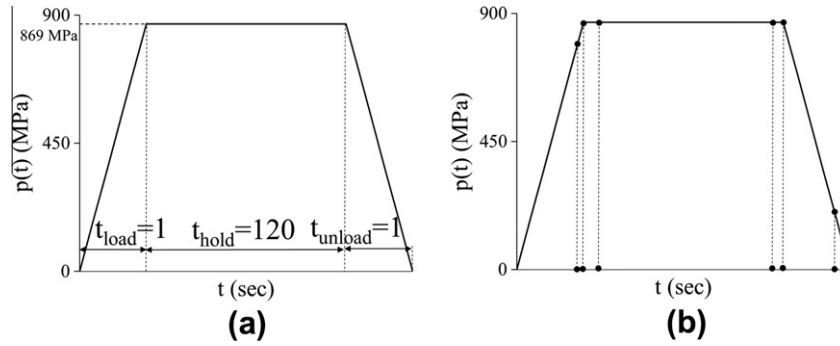


Fig. 9. Schematic of cyclic dwell loading: (a) dwell load profile applied on y-face of the polycrystalline microstructure (b) segments with different maximum resolution.

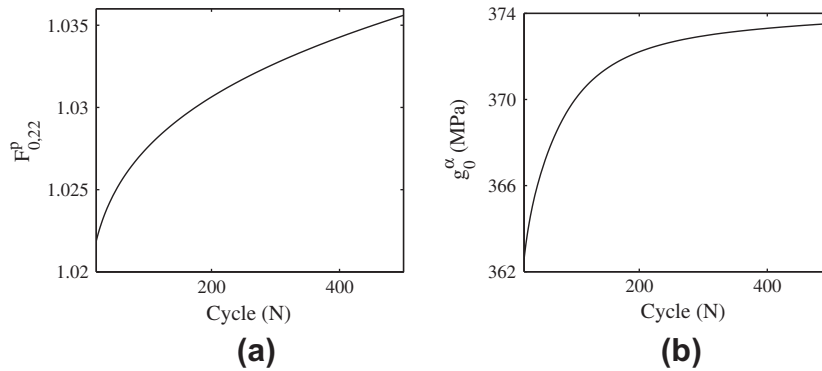


Fig. 10. Evolution of cycle-scale internal variables at an integration point in the microstructure: (a)  $F_{0.22}^p$  (b) one of the slip system resistances  $g_0^\alpha$ .

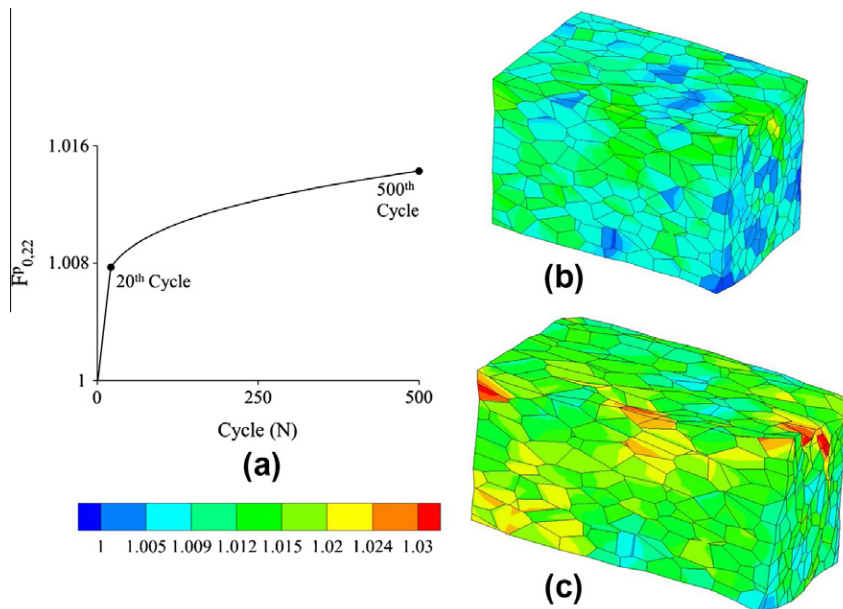


Fig. 11. Evolution of  $F_{0.22}^p$  with cycles by the WATMUS based CPFEM simulations: (a) volume averaged  $F_{0.22}^p$ , (b) distribution of  $F_{0.22}^p$  at the 21st cycle, (c) distribution of  $F_{0.22}^p$  at the 500th cycle.

of cycles to crack nucleation from interrupted dwell fatigue experiments is 550 cycles. From the CPFE simulations, the number of cycles to crack nucleation is predicted for 80% and 85% respectively of the total life as:

$$N_{c(80\%)} : \max_{\alpha} R_{\alpha}(N, \tau = 121 \text{ s}) = R_{c(80\%)} \Rightarrow N_{c(80\%)} = 620$$

$$N_{c(85\%)} : \max_{\alpha} R_{\alpha}(N, \tau = 121 \text{ s}) = R_{c(85\%)} \Rightarrow N_{c(85\%)} = 694 \quad (29)$$

The evolution of maximum  $R_{\alpha}$  at a grain boundary node with crack nucleation is shown in Fig. 18.

The predicted number of cycles to crack nucleation for specimen 2 along with the associated error are summarized in Table 1. The crystallographic features of the predicted crack nucleation site for both the specimens are compared with experimentally observed characteristics in Table 2.

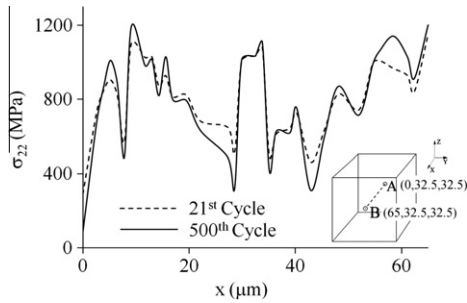


Fig. 12. Evolution of loading direction stress component  $\sigma_{22}$  along a material line in the microstructure evaluated at cycles  $N = 21$  and  $N = 500$  and  $\tau = 121$  s.

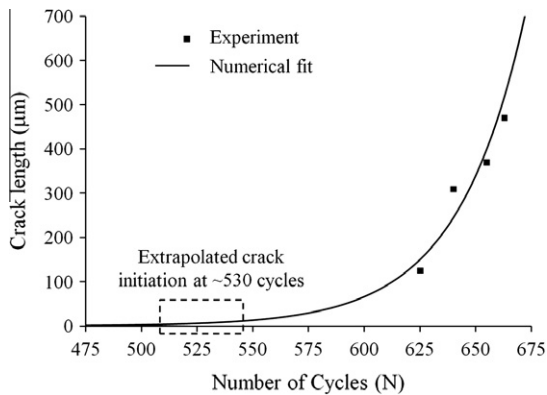


Fig. 13. Sub-surface crack propagation in specimen #2 obtained from ultrasonic experiments and corresponding number of cycles to nucleation [3].

Contour plots of  $\sigma_{22}$ ,  $F_{22}^p$  and the  $\langle c \rangle$ -axis orientation on a microstructural section of specimen 2, containing a crack nucleation site are shown in Fig. 19. The variables are evaluated for cycle  $N = 620$  and intra-cycle time  $\tau = 121$  s. Crack nucleation is predicted near the triple point of grains 1, 2 and 3, shown in Fig. 19a. From the distribution of  $\langle c \rangle$ -axis orientation  $\theta_c$  at the crack nucleation site (CNS) in Fig. 19a, it is observed that the grain labeled 1 has  $\theta_c < 30^\circ$  and is hence the hard grain. As seen in Fig. 19b, this grain undergoes reduced plastic deformation in comparison with the surrounding soft grains, for which  $\theta_c > 40^\circ$  in Fig. 19a. The presence of large soft grains surrounding grain 1 cause large stresses develop in the hard grain as seen in Fig. 19c. This causes nucleation of a crack at its interface with grains 2 and 3.

Two important inferences can be made from Fig. 19. The first is that the  $\langle c \rangle$ -axis orientation has a strong influence on the local evo-

lution of crystal plasticity variables, and can be used to distinguish between hard and soft grains. The second is that the local hard-soft grain arrangements can be used to examine the sensitivity of crack nucleation life on the microstructure.

## 6. Influence of microstructural and loading characteristics on crack nucleation in Ti-6242

Quantitative correlation of microstructural and loading characteristics to the fatigue life using computational models can improve life prediction capabilities as well as provide tools for microstructure design [47,48]. Experimental studies have been performed by various authors to identify different factors that influence the fatigue life of Ti-alloys. The effect of colony structure on room temperature low cycle fatigue behavior of  $\beta$ -processed and  $\beta$ -annealed Ti-alloys has been investigated in [49]. Selected area electron channeling has been used in [50] to identify the crystallography of flat facets on the fracture surfaces of  $\alpha/\beta$  Ti-alloys under fatigue loading. Near basal facet orientation has been observed at the crack nucleation site in [7,41,40]. Similar studies have been performed in [51,5,6,52] to relate microstructure, texture and operating conditions to room temperature fatigue life of  $\alpha/\beta$  Ti-alloys.

In recent years, an integrated experimental and computational approach has been pursued by authors to incorporate experimental observations into failure models for improved understanding and life prediction abilities. Extreme value statistics in conjunction with CPFE simulations have been used in [53,54] to obtain microstructure dependent high cycle fatigue failure probabilities in Ti-6Al-4V. In this section a similar attempt has been made to relate room temperature crack nucleation in Ti-6242 to microstructural features and loading profile under cyclic loading using the WATMUS method-enhanced CPFE simulations.

### 6.1. Sensitivity of yield strength to grain orientation and size distributions

The yield strength of a polycrystalline alloy depends on the plastic flow behavior of the individual grains. Room temperature plastic deformation in Ti-6242 is primarily due to slip in individual grains. Consequently, factors affecting initiation of slip are used to study the sensitivity of yield strength to the underlying microstructure. Functional relations between microstructural characteristics such as grain orientation and size distribution and the yield strength have been established in [20,34]. From Eq. (3), the initiation of slip is directly related to the resolved shear stress  $\tau^z$  and inversely related to the slip system resistance  $g^z$ . The resolved shear

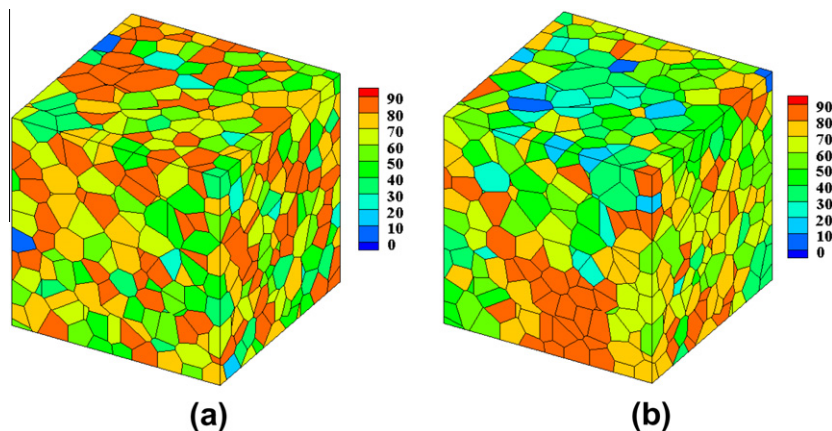


Fig. 14. Statistically equivalent image-based simulated polycrystalline microstructures and corresponding  $\langle c \rangle$ -axis orientations for: (a) specimen 1 and (b) specimen 2.

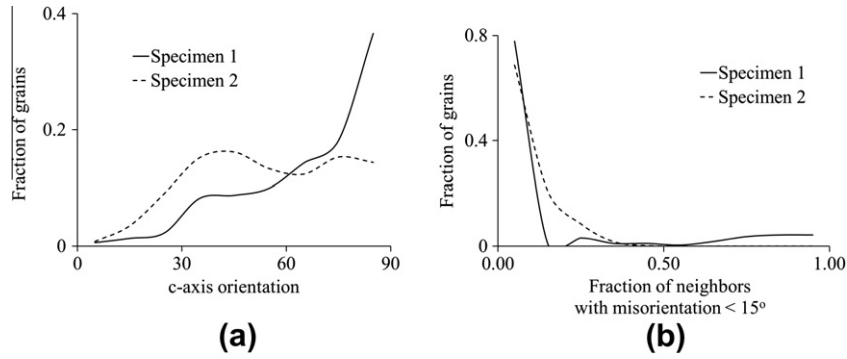


Fig. 15. (a) (c)-axis orientation distribution and (b) microtexture distribution for statistically equivalent specimen microstructures 1 and 2.

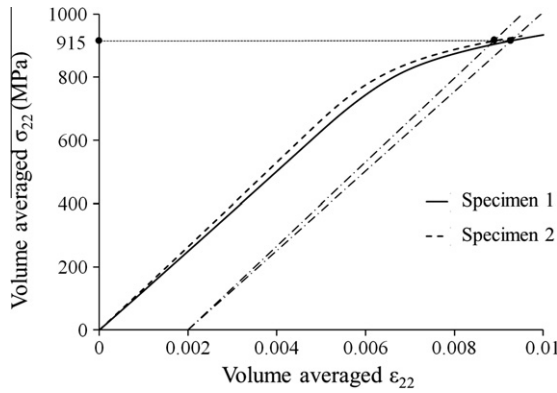


Fig. 16. Volume averaged stress–strain plot of statistically equivalent microstructures obtained from constant strain rate CPFEM simulations. A yield stress of 915 MPa is obtained for 0.2% elastic strain.

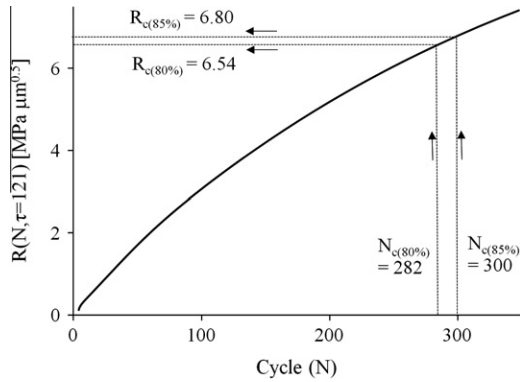


Fig. 17. Evolution of nodal  $R_z$  with cycles  $N$  in specimen 1 at the crack nucleation site under dwell loading, evaluated at  $\tau = 121$  s.

stress, in turn depends on the orientation of the grain with respect to the direction along which yield strength is measured. The slip system resistance  $g_0^z$  depends on the type of slip system, i.e.  $\langle a \rangle$ -basal,  $\langle a \rangle$ -prismatic,  $\langle a \rangle$ -pyramidal,  $\langle c + a \rangle$  pyramidal and the grain size from Eq. (12).

Plastic deformation in a grain of a given size and orientation with the loading direction, is represented by a parameter termed as the *Plastic Flow Index* or *PFI*, defined as:

$$PFI = \max_{\alpha} \left( \frac{|\cos \theta_n^{\alpha} \cos \theta_m^{\alpha}|}{0.5} \right) \left( \frac{g_0^{prismatic}}{g^z} \right) \quad (30)$$

where  $\theta_n^{\alpha}$  and  $\theta_m^{\alpha}$  are the angles made by the slip plane normals and the corresponding slip directions with the loading direction.  $g_0^{prismatic}$

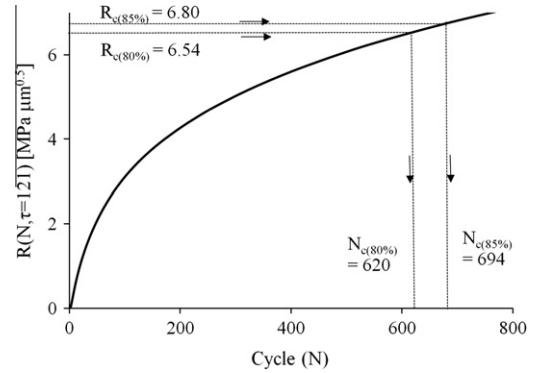


Fig. 18. Evolution of maximum  $R_z$  with  $N$  in specimen 2 at a crack nucleation site under dwell cyclic loading, evaluated at  $\tau = 121$  s.

is the slip system resistance of the prismatic  $\langle a \rangle$  slip system in Eq. (12) and its value is taken from [23]. The calibrated value of  $g_0$  in [23] is the smallest for the prismatic  $\langle a \rangle$  slip system. Hence, it is considered as a reference in Eq. (30) since it implies least resistance to slip. A crystal oriented with the maximum Schmid factor 0.5 along the prismatic  $\langle a \rangle$  slip system has the minimum yield strength and maximum plastic flow, compared to any other grain orientation. Thus the *PFI* is considered to provide an effective measure of plastic flow in the grain. It also depends on the loading direction or Schmid factor of individual slip systems in the grain. The *PFI* has characteristics similar to the Taylor factor in [7] in that it uses a measure of the slip rate to determine the degree of plasticity in each grain of the polycrystalline microstructure. However there are also some distinct differences, viz.

- The maximum ratio from all the slip systems in a grain is considered in *PFI*.
- The microstructure with maximum slip activity (single crystal with SF = 0.5 on prismatic slip system) is considered to obtain the relative measure *PFI*.
- The distribution of *PFI* instead of a volume average is used to obtain a relative measure of yield strength for polycrystalline alloys.

For a grain, the value of *PFI* can vary between 0 and 1, i.e.  $0 \leq PFI < 1$ . A higher value of *PFI*, i.e.  $PFI \rightarrow 1$  indicates higher plastic flow and lower strength for the grain. The yield strengths of specimens 1 and 2 in the  $y$ -direction are related to the underlying grain sizes and orientations by considering the *PFI* distribution of individual grains in the microstructure. The distributions are compared in Fig. 20.

**Table 1**  
Comparison of the number of cycles to crack nucleation predicted by the model with experimental results for specimen 2.

Cycles to crack nucleation (experiment)	Cycles to crack nucleation (predicted)		% Relative error	
	80% of life	85% of life	80% of life	85% of life
550	620	694	12.7	25.4

**Table 2**  
Crystallographic features of the crack nucleation site predicted by the model and experiments for specimens 1 and 2.

Microstructural parameters	Experiments	Specimen 1	Specimen 2
$\theta_c$ (°)	0–30	38.5	25.2
Prismatic Schmid factor	0.0–0.1	0.17	0.09
Basal Schmid factor	0.3–0.45	0.48	0.38

The distributions show that both specimens 1 and 2 have similar high volume fractions ( $VF \approx 0.2$ ) in the range  $0.7 \leq PFI < 0.8$ . Constant strain-rate CPFEM simulation results in Fig. 16 also show similar yield strengths in the y-direction for these specimens. The *PFI* distribution provides an effective metric in relating the yield strength to the underlying grain sizes and orientations. To validate this postulate, a third virtual microstructure (specimen 3) is constructed by randomly assigning orientations to grains in the FE model of Fig. 2a. The orientations are chosen from the set of orientations in specimen 1. The grain sizes of specimen 3 are the same as for specimen 1. The *PFI* distribution for specimen 3 is compared with those for specimens 1 and 2 in Fig. 20. This has a lower volume fraction in the range  $0.7 \leq PFI < 0.8$ . Correspondingly, specimen 3 is expected to have a higher yield strength. This is corroborated by constant strain-rate CPFEM simulation results, for which the yield strength is 940 MPa. Since  $\cos \theta_n^z \cos \theta_m^z$  in Eq. (30) depends on the direction of loading, the *PFI* distributions for different loading directions capture the anisotropy in the macroscopic response as well.

## 6.2. Sensitivity of crack nucleation to microstructural features

Macroscopic descriptors such as the *Plastic Flow Index* distribution are unable to capture the local variations in grain orientations and sizes. Hence, they are not suitable for relating variations in microstructural features to the fatigue nucleation life. Crystallographic features at the crack nucleation site, obtained from fatigue experiments on Ti-6242 in [41,40] are reported in Table 2. This data can be used to capture the effect of local variations in microstructural features on the number of cycles to fatigue crack nucleation. Grains are distinguished as hard or soft, based on their  $\langle c \rangle$ -axis orientation with respect to the loading axis. Orientations between  $0^\circ$  and  $30^\circ$  ensures that the maximum prismatic and basal  $\langle a \rangle$  Schmid factors are in the range 0.0–0.1 and 0.3–0.45 respectively, as shown in Fig. 21.

The  $\langle c \rangle$ -axis orientation at the crack nucleation site for specimen 1 is predicted to be  $38.5^\circ$  by the crack nucleation model. Consequently, a  $\langle c \rangle$ -axis orientation range of  $0$ – $40^\circ$  is used here to identify hard and soft grains. A grain is assumed to be hard when its  $\langle c \rangle$ -axis orientation with respect to the loading direction is less than  $40^\circ$ . Since hard grains surrounded by soft grains are more susceptible to crack nucleation, the surface area fraction of soft grains surrounding each hard grain or *SAFSSG* is examined as a potential metric. The distribution of *SAFSSG* for specimens 1, 2 and 3 is shown in Fig. 22.

The number of cycles to crack nucleation depends on the extreme values of the distribution in Fig. 22. This implies that a microstructure with a higher volume fraction of hard grains with

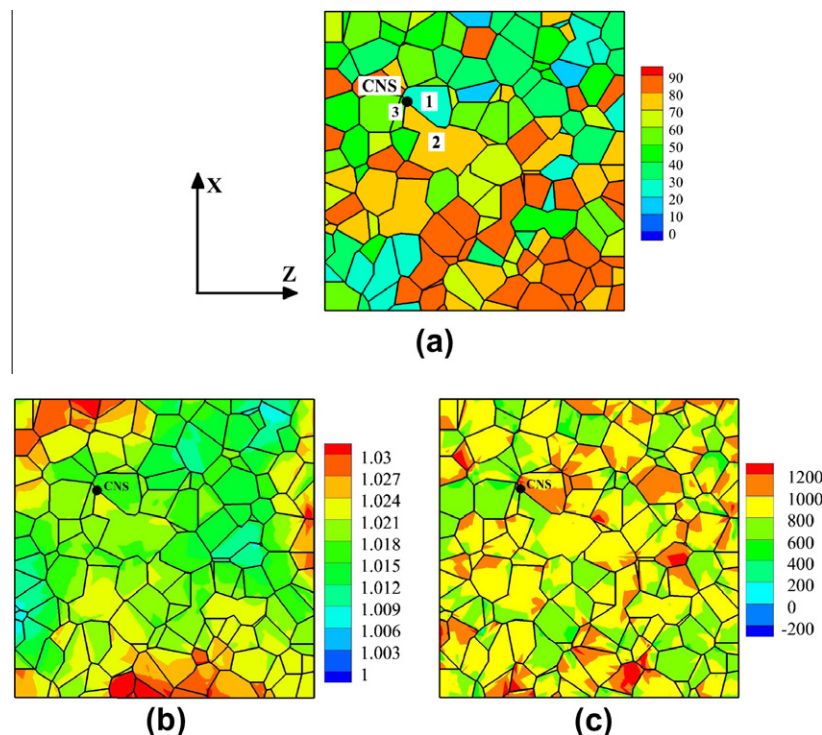


**Fig. 19.** Contour plots of (a)  $\langle c \rangle$ -axis orientation, (b)  $F_{22}^p$  and (c)  $\sigma_{22}$  on a section of specimen 2 containing the predicted crack nucleation site. The CPFEM variables are at  $N = 620$  and  $\tau = 121$  s.

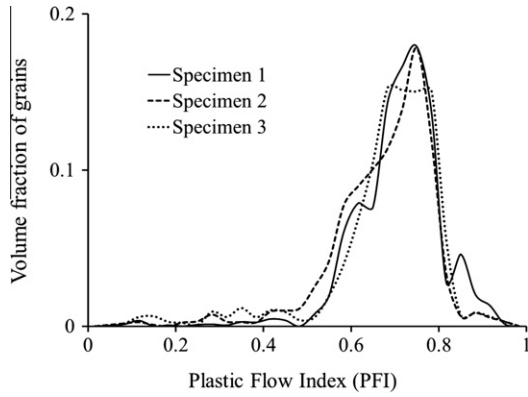


Fig. 20. Plastic Flow Index (PFI) distribution for specimens 1, 2 and 3.

high SAFSSG is likely to nucleate cracks earlier. Fig. 22 illustrates that specimen 2 should have the longest nucleation life and specimen 3 should have the shortest life. This observation is supported by dwell fatigue simulations and experiments for specimens 1 and 2.

To consolidate this observation, dwell fatigue simulations are performed on specimen 3 with a maximum applied stress of 894 MPa, corresponding to 95% of its macroscopic yield stress of 940 MPa. The crack nucleation parameter  $R_x$  is evaluated at all nodes at grain interfaces in every cycle  $N$  for  $\tau = 121$  s. Crack nucleation is considered to happen when  $R_x(N, \tau = 121$  s) at any node exceeds a critical value  $R_c$ . The predicted number of cycles to crack nucleation, corresponding to nucleation at 80% or 85% of total life, are  $N_{c(80\%)} = 167$  and  $N_{c(85\%)} = 177$  respectively. The microstructural features observed at the predicted crack nucleation site for specimen 3 are shown in Table 3. The evolution of  $R_x$  at the predicted crack nucleation site for the three different microstructures are compared in Fig. 23.

A comparison of cycles to crack nucleation for different volume fraction (VF) of hard grains with increasing surface area fraction SAFSSG between 0.9 and 1 is shown in Fig. 24.

6.3. Sensitivity of crack nucleation to characteristics of applied loading

Specimen 3 is subjected to four different loading cases for this sensitivity study, viz.:

- Case A:  $\sigma_{max} = 894$  MPa,  $\sigma_r = 0$ ,  $T_{load} = T_{unload} = 1$ sec and  $T_{hold} = 120$  s.
- Case B:  $\sigma_{max} = 847$  MPa,  $\sigma_r = 0$ ,  $T_{load} = T_{unload} = 1$ sec and  $T_{hold} = 120$  s.

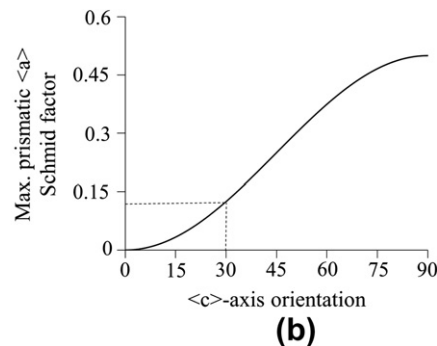
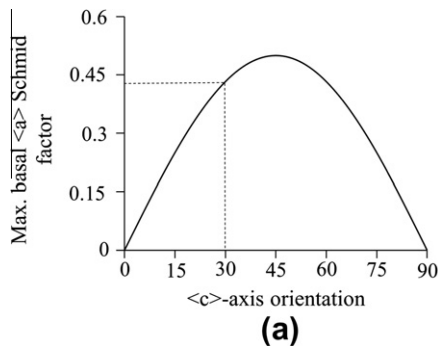


Fig. 21. Variation of slip system Schmid factors with <c>-axis orientation: (a) maximum basal (a) Schmid factor (b) maximum prismatic (a) Schmid factor.

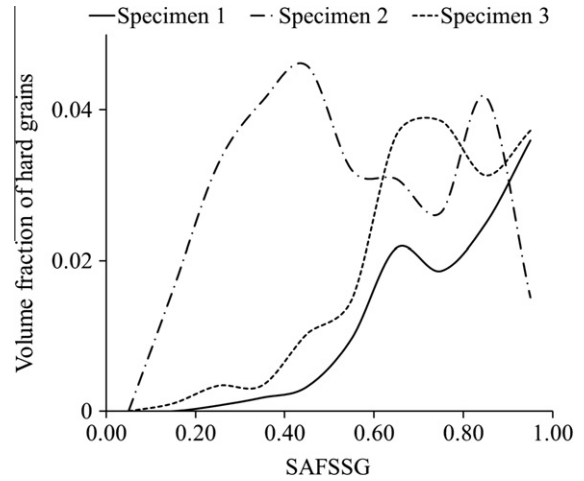


Fig. 22. Volume fraction distribution of hard grains and corresponding surface area fractions of surrounding soft grains (SAFSSG) in specimens 1, 2 and 3.

- Case C:  $\sigma_{max} = 894$  MPa,  $\sigma_r = 0$ ,  $T_{load} = T_{unload} = 61$ sec and  $T_{hold} = 0$  s.
- Case D:  $\sigma_{max} = 894$  MPa,  $\sigma_r = 0$ ,  $T_{load} = T_{unload} = 1$ sec and  $T_{hold} = 0$  s.

The maximum applied stress  $\sigma_{max}$  is 95% of yield strength for cases A, C and D, while it is 90% for case B. Dwell load with 2 min hold is applied in cases A and B. Triangular loading with time periods  $T = 122$  s and  $T = 2$  s are respectively applied for cases C and D. The WATMUS method is used to perform cyclic CPFEM simulations and the crack nucleation parameter  $R_x$  is evaluated at nodes on the grain boundaries. Within a cycle,  $R_x$  is evaluated at the beginning of unloading. This corresponds to  $\tau = 121$  s for cases A and B,  $\tau = 61$  s for case C and  $\tau = 1$  s for case D. The evolution of  $R_x$  at the node, where crack nucleation is predicted, is shown in Fig. 25.

The predicted number of cycles to crack nucleation based on the calibrated  $R_c$  values are summarized in Table 4. The microstructure has a shorter life when subjected to dwell loading cases A and B in comparison with normal cyclic loading cases C and D. For the latter cases, a decrease in loading frequency reduces life. The number of cycles to crack nucleation for dwell case A and normal fatigue case D at 95% of yield strength shows the same trend as observed experimentally in [5–7].

In every dwell cycle, the microstructure is held at the maximum stress level for a longer period of time than in the normal cyclic loading. This results in a larger inelastic deformation and strain accumulation in the microstructure within each dwell cycle. Similar observations have been made from experiments on Ti-6242 in

**Table 3**  
Microstructural features at the predicted crack nucleation site for specimen 3.

Microstructural parameters	Experiments	Specimen 3
$\theta_c$ (°)	0–30	5.6
Prismatic Schmid factor	0.0–0.1	0.005
Basal Schmid factor	0.3–0.45	0.01

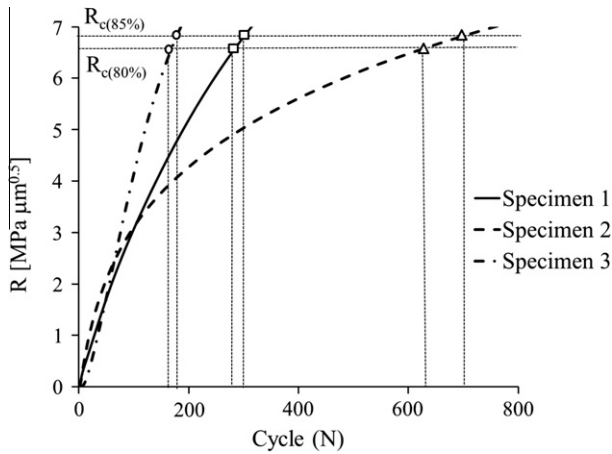


**Fig. 23.** Evolution of  $R$  at the predicted crack nucleation site for specimens 1, 2 and 3.

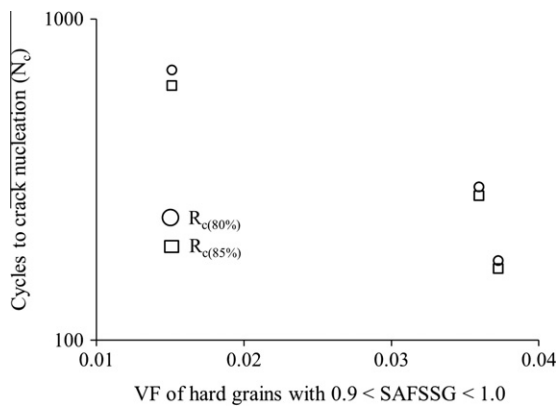


**Fig. 24.** Comparison of number of cycles to crack nucleation for different volume fraction (VF) of hard grains with surface area fraction of surrounding soft grains (SAFSSG) between 0.9 and 1.

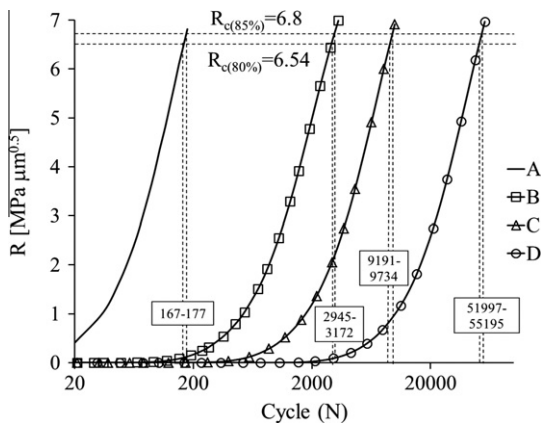


**Fig. 25.** Evolution of  $R_z$  with cycles at the predicted crack nucleation site for specimen 3, under four different fatigue loading cases described in Section 6.3.

[7] and Timetal 685 in [5]. Stress concentration and micro-crack growth at the hard soft grain interface are more pronounced in every cycle for the dwell loading. This explains the reduction in life to crack nucleation under dwell load of case A when compared to normal cyclic load of case D. A reduction in the maximum applied stress in dwell loading for case B reduces the cyclic strain accumulation and the accompanying stress rise. Consequently, it shows a

**Table 4**  
Comparison of number of cycles to crack nucleation in specimen 3 for different cyclic loadings.

Case no.	Cycles to crack nucleation	
	80% of life	85% of life
A	167	177
B	2945	3172
C	9191	9734
D	51,997	55,195

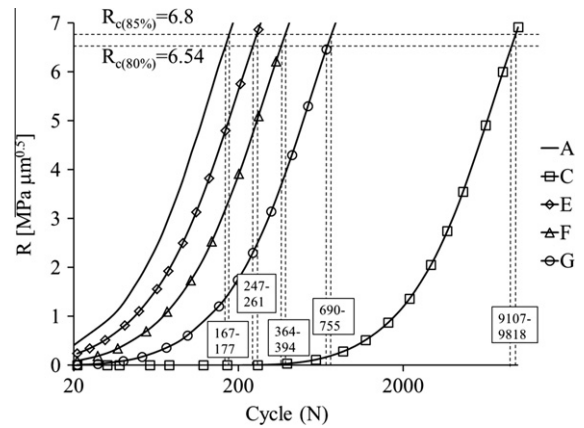


**Fig. 26.** Evolution of  $R_z$  with cycles at the crack nucleation site of specimen 3 for the fatigue loading cases A, C, E, F and G.

**Table 5**  
Number of cycles to crack nucleation in specimen 3 for dwell cyclic load with different hold times.

Case no.	Cycles to crack nucleation	
	80% of life	85% of life
E	247	261
F	364	394
G	690	755

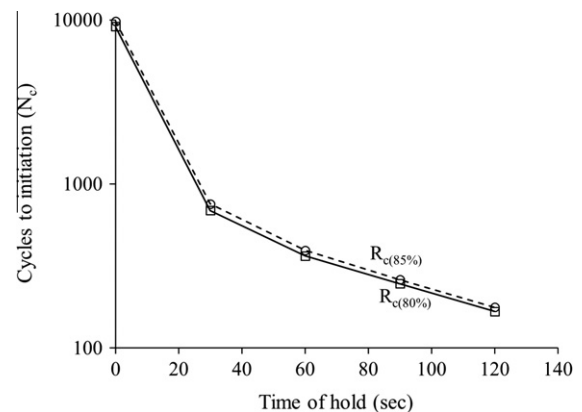


**Fig. 27.** Number of cycles to crack nucleation in specimen 3 for different hold times.

longer life than case A. When the frequency of normal cyclic loading is reduced in case C, ramping to the maximum applied stress in every cycle happens slowly. This results in increased plastic strain accumulation and stress rise, compared to the higher frequency case D. Thus, frequency reduction for the same maximum stress level decreases the nucleation life of the microstructure.

The number of cycles to crack nucleation for specimen 3 for different hold, loading and unloading times in dwell cyclic loading are also compared. The applied stress levels are kept at  $\sigma_{max} = 894$  MPa and  $\sigma_{min} = 0$  MPa, while the total period of loading is  $T = 122$  s. The WATMUS based CPFEM simulations are performed for three different cases, viz.:

- Case E:  $T_{load} = T_{unload} = 16$  s and  $T_{hold} = 90$  s.
- Case F:  $T_{load} = T_{unload} = 31$  s and  $T_{hold} = 60$  s.
- Case G:  $T_{load} = T_{unload} = 46$  s and  $T_{hold} = 30$  s.

The number of cycles to nucleate a crack is evaluated and the nodal  $R_x$  at the predicted crack nucleation site is evaluated at  $\tau = 106$  s, 91 s and 76 s respectively within the cyclic increments. This is shown in Fig. 26. The number of cycles to crack nucleation for cases E, F and G are summarized in Table 5. With increasing hold time, the dislocation pile-up length at the hard-soft grain boundaries and stress-peak in the hard grains has a larger increase in every load cycle, resulting in shorter life to initiation. A comparison of the number of cycles to crack nucleation for different hold times is shown in Fig. 27.

## 7. Conclusion

This paper investigates the effects of critical morphological and crystallographic characteristics of the microstructure and loading conditions on grain-level crack nucleation in polycrystalline Ti-6242 microstructures. Crystal plasticity FEM simulations of statistically equivalent microstructures, in conjunction with a physically motivated crack nucleation model, are used to provide a mechanistic approach towards predicting this behavior. A non-local crack nucleation model in terms of the local stresses near the hard grain boundary and the piled-up dislocations in the adjacent soft grain is implemented to predict nucleation in the hard grain. Crack nucleates when a parameter  $R$  at any node on hard soft grain interfaces exceeds a critical value  $R_c$  for the material. This critical parameter value is calibrated using a combination of dwell fatigue experiments and CPFEM simulations performed on Ti-6242 specimens. It is practically impossible to conduct CPFEM simulations till the incidence of crack nucleation for many microstructures and load cases, using conventional single time-scale simulation methods. A necessary ingredient of these simulations is the wavelet transformation induced multi-time scaling or WATMUS algorithm for accelerated cyclic CPFEM simulations.

Crack nucleation studies are performed for cyclic loads with the maximum applied stress levels at 90–95% of the macroscopic yield strength. To understand the effect of microstructural characteristics on the fatigue crack nucleation behavior, the dependence of yield strength on the underlying grain orientations and sizes is developed through the introduction of an effective microstructural parameter *Plastic Flow Index* or *PFI*. The *PFI* distribution is found to provide a good measure of the yield strength for a microstructure. However, this distribution is not suitable to undermine the effects of the microstructure on crack nucleation, since it is a *local* event. Hence a local microstructural variable is defined in terms of the neighborhood of the hard grains. Specifically the surface area fraction of soft grains surrounding each hard grain or SAFSSG is used to establish the microstructural sensitivity of cycles to crack nucleation. The WATMUS-based CPFEM simulations of three representa-

tive microstructures are performed under cyclic dwell loading and the cycles to crack nucleation are predicted. The results confirm the effectiveness of the SAFSSG in capturing the influence of microstructure on cycles to crack nucleation. Furthermore, simulations with different cyclic load patterns suggest that fatigue crack nucleation in Ti-6242 strongly depends on the dwell cycle hold time at maximum stress. This is in compliance with experimental observations.

## Acknowledgments

This work has been partially supported by the Air Force Office of Scientific through a Discovery Challenge Grant (DCT Grant # FA-9550-09-1-045 2, Program Manager: Dr. David Stargel) and by the National Science Foundation, Mechanics and Structure of Materials Program through Grant No. CMMI-0800587 (Program Director: Dr. Clark Cooper). This sponsorship is gratefully acknowledged.

## References

- [1] Joseph DS, Chakraborty P, Ghosh S. Wavelet transformation based multi-time scaling for crystal plasticity FE simulations under cyclic loading. *Comput Methods Appl Mech Eng* 2010;199:2177–94.
- [2] Chakraborty P, Joseph DS, Ghosh S. Wavelet transformation based multi-time scale crystal plasticity FEM for cyclic deformation in titanium alloys under dwell load. *Fin Elem Anal Des* 2011;47:610–8.
- [3] Anahid M, Samal MK, Ghosh S. Dwell fatigue crack nucleation model based on crystal plasticity finite element simulations of polycrystalline titanium alloys. *J Mech Phys Solids* 2011;59(10):2157–76.
- [4] Sinha S, Ghosh S. Modeling cyclic ratcheting based fatigue life of HSLA steels using crystal plasticity fem simulations and experiments. *Int J Fatigue* 2006;28:1690–704.
- [5] Bache MR. A review of dwell sensitive fatigue in titanium alloys: the role of microstructure, texture and operating conditions. *Int J Fatigue* 2003;25:1079–87.
- [6] Bache MR, Cope M, Davies HM, Evans EJ, Harrison G. Dwell sensitive fatigue in a near alpha titanium alloy at ambient temperature. *Int J Fatigue* 1997;19(93):83–8.
- [7] Sinha V, Mills MJ, Williams JC. Understanding the contributions of normal-fatigue and static loading to the dwell fatigue in a near-alpha titanium alloy. *Metall Mater Trans A* 2004;35:3141–8.
- [8] Goh CH, Wallace JM, Neu RW, McDowell DL. Polycrystal plasticity simulations of fretting fatigue. *Int J Fatigue* 2001;23:5423–35.
- [9] Sackett E, Germain L, Bache M. Crystal plasticity, fatigue crack initiation and fatigue performance of advanced titanium alloys. *Int J Fatigue* 2007;29:2015–21.
- [10] Bridiera F, McDowell DL, Villechaise P, Mendez J. Crystal plasticity modeling of slip activity in Ti-6Al-4V under high cycle fatigue loading. *Int J Plast* 2009;25:1066–82.
- [11] Mineur M, Villechaise P, Mendez J. Influence of the crystalline texture on the fatigue behavior of a 316L austenitic stainless steel. *Mater Sci Eng* 2000;A286:257–68.
- [12] McDowell D, Dunne FPE. Microstructure-sensitive computational modeling of fatigue crack formation. *Int J Fatigue* 2010;32:1521–42.
- [13] Suresh S. *Fatigue of materials*. Cambridge: Cambridge University Press; 1998.
- [14] Laird CM. *The fatigue limit of metals*. *Mater Sci Eng* 1976;22:231–6.
- [15] Fleck NA, Kang KJ, Ashby MF. The cyclic properties of engineering materials. *Acta Met Mater* 1994;42:365–81.
- [16] Hashimoto TM, Pereira MS. Fatigue life studies in carbon dual-phase steels. *Int J Fatigue* 1996;18(8):529–33.
- [17] Coffin LF. *Fatigue*. *Annu Rev Mater Sci* 1973;2:313–48.
- [18] Paris PC. *The fracture mechanics approach to fatigue, fatigue an interdisciplinary approach*. Syracuse: Syracuse University Press; 1964.
- [19] Hasija V, Ghosh S, Mills MJ, Joseph DS. Modeling deformation and creep in Ti-6Al alloys with experimental validation. *Acta Mater* 2003;51:4533–49.
- [20] Deka D, Joseph DS, Ghosh S, Mills MJ. Crystal plasticity modeling of deformation and creep in polycrystalline Ti-6242. *Metall Trans A* 2006;37(5):1371–88.
- [21] Gong J, Wilkinson A. Anisotropy in the plastic flow properties of single-crystal alpha titanium determined from micro-cantilever beams. *Acta Mater* 2009;57:5693–705.
- [22] Lutjering G, Williams JC. *Titanium*. Berlin-Heidelberg: Springer-Verlag; 2007.
- [23] Venkatramani G, Ghosh S, Mills MJ. A size dependent crystal plasticity finite element model for creep and load-shedding in polycrystalline titanium alloys. *Acta Mater* 2007;55:3971–86.
- [24] Groeber M, Ghosh S, Uchid MD, Dimiduk DM. A framework for automated analysis and simulation of 3d polycrystalline microstructures. Part 1: Statistical characterization. *Acta Mater* 2008;56:1257–73.

- [25] Groeber M, Ghosh S, Uchic MD, Dimiduk DM. A framework for automated analysis and simulation of 3d polycrystalline microstructures. Part 2: Synthetic structure generation. *Acta Mater* 2008;56:1274–87.
- [26] Bennett VP, McDowell DL. Polycrystal orientation distribution effects on microslip in high cycle fatigue. *Int J Fatigue* 2003;25:27–39.
- [27] Turkmen HS, Loge RE, Dawson PR, Miller M. On the mechanical behavior of aa 7075-t6 during cyclic loading. *Int J Fatigue* 2003;25:267–81.
- [28] Blekhan II. *Vibrational mechanics*. World Scientific; 2000.
- [29] Thomsen JJ. *Vibrations and stability: theory, analysis and tools*. 2nd ed. Berlin: Springer-Verlag; 2004.
- [30] Yu Q, Fish J. Temporal homogenization of viscoelastic and viscoplastic solids subjected to locally periodic loading. *Comput Mech* 2002;29:199–211.
- [31] Manthiraju S, Asai M, Ghosh S. A dual time scale finite element model for simulating cyclic deformation of polycrystalline alloys. *J Strain Anal Eng Des* 2007;42:183–200.
- [32] Oskay C, Fish J. Multiscale modeling of fatigue for ductile materials. *Int J Multiscale Comput Eng* 2004;2:1–25.
- [33] Oskay C, Fish J. Fatigue life prediction using 2-scale temporal asymptotic homogenization. *Int J Numer Methods Eng* 2004;61:329–59.
- [34] Venkatramani G, Deka D, Ghosh S. Crystal plasticity based fe model for understanding microstructural effects on creep and dwell fatigue in Ti-6242. *ASME J Eng Mater Tech* 2006;128(3):356–65.
- [35] Kalidindi SR, Bronkhorst CA, Anand L. Crystallographic texture evolution in bulk deformation processing of fcc metals. *J Mech Phys Solids* 1992;40:537–69.
- [36] Anand L, Kothari M. A computational procedure for rate-independent crystal plasticity. *J Mech Phys Solids* 1996;44(4):525–58.
- [37] Balasubramanian S, Anand L. Elasto-viscoplastic constitutive equations for polycrystalline fcc materials at low homologous temperatures. *J Mech Phys Solids* 2002;50(1):101–26.
- [38] Morrissey RJ, McDowell DL, Nicholas T. Microplasticity in HCF of Ti-6Al-4V. *Int J Fatigue* 2001;23:S55–64.
- [39] Acharya A, Beaudoin AJ. Grain-size effect in viscoplastic polycrystals at moderate strains. *J Mech Phys Solids* 2000;48:2213–30.
- [40] Sinha V, Spowart JE, Mills MJ, Williams JC. Observations on the faceted initiation site in dwell-fatigue tested Ti-6242 alloy: crystallographic orientation and size effects. *Metall Mater Trans A* 2006;37:1507–18.
- [41] Sinha V, Mills MJ, Williams JC. Crystallography of fracture facets in a near-alpha titanium alloy. *Metall Mater Trans A* 2006;37:2015–26.
- [42] Stroh AN. The formation of cracks as a result of plastic flow. *Proc Roy Soc London, Ser A* 1954;223:404–14.
- [43] Walker J. *A primer on wavelets and their scientific applications*. CRC Press; 1999.
- [44] Strang G, Nguyen T. *Wavelets and filter banks*. Wellesley College; 1996.
- [45] Rokhlin S, Kim JY, Zoofan B. unpublished research 2005. The Ohio State University; 2005.
- [46] Ghosh S, Bhandari Y, Groeber M. Cad-based reconstructed 3D polycrystalline alloy microstructures from fib generated serial sections. *Comput Aid Des* 2008;40:293–310.
- [47] Olson GB. Computational design of hierarchically structured materials. *Science* 1997;277:1237–42.
- [48] Adams BL, Henrie A, Henrie B, Lyon M, Kalidindi SR, Garmestani H. Microrstructure-sensitive design of a compliant beam. *J Mech Phys Solids* 2001;49:1639–63.
- [49] Eylon D, Hall JA. Fatigue behavior of beta processed titanium alloy imi 685. *Met Trans A* 1977;8A:981–90.
- [50] Davidson DL, Eylon D. Titanium alloy fatigue fracture facet investigation by selected area electron channeling. *Mat Trans A* 1980;11A:837–43.
- [51] Bache MR, Evans WJ, Suddell B, Herrouin FRM. The effects of texture in titanium alloys for engineering components under fatigue. *Int J Fatigue* 2001;23:153–9.
- [52] Evans WJ. Optimising mechanical properties in alpha+beta titanium alloys. *Mater Sci Eng A* 1998;243:89–96.
- [53] Przybyla CP, McDowell DL. Microstructure-sensitive extreme value probabilities for high cycle fatigue of Ti-6Al-4V. *Int J Plast* 2011;27:1871–95.
- [54] Przybyla CP, McDowell DL. Microstructure-sensitive extreme-value probabilities of high-cycle fatigue for surface vs. subsurface crack formation in duplex Ti-6Al-4V. *Acta Mater* 2012;60:293–305.